Progressive compaction of soft cellular structures with layer-wisely designed gradient porosity

Fei Wang [a], D.M. Li [a, b, *], Yi-Ru Yang [a], Zhangming Wu [c]

a. School of Civil Engineering and Architecture, Wuhan University of Technology, Wuhan, 430070, China

b. School of Science, Wuhan University of Technology, Wuhan, 430070, China

c. School of Engineering, Cardiff University, Wales, UK, CF24 3AA

Abstract: Soft cellular structures possess excellent recoverable compacting characteristics, which have great potentials for developing a new branch of flexible metamaterials with emerging applications. Inspired by the microstructures of natural materials, a novel type of soft cellular structures with gradient porosity, which are different from the periodic cellular structures, is proposed and designed in this study. In this new design of soft cellular structures, the overall porosity is kept as a constant while the porosity is varying along each layer gradually. In doing so, a new kind of soft cellular structures possess a layer-wisely designed gradient porosity is achieved. This design enables the cellular structures to exhibit a distinct progressive compaction behavior which is completely different from the uniform densification of the soft periodic structures. The progressive compaction of the structure is controllable through designing the gradient of the porosity to regulate stiffness of each layer. The mechanical responses and properties of the gradient soft cellular structures with different porosities and different layer-wise patterns under uniaxial compression are investigated both experimentally and numerically. This study reveals that the maximum absolute values of negative Poisson's ratio of current gradient soft cellular structures is 2.113 time than that of periodic ones with a same overall porosity. The additional design freedom introduced by porosity gradient is beneficial for adjusting the mechanical properties of soft cellular metamaterials to meet the design demands of various potential applications.

Keywords: Soft cellular structures, gradient porosity, progressive compaction, negative Poisson’s ratio, metamaterials

* Corresponding author.
E-mail addresses: dongmli2-c@my.cityu.edu.hk (D.M. Li), domili@whut.edu.cn (D.M. Li)

1. Introduction

Cellular structures like honeycombs [1], foams [2], and lattices [3] etc. that consist of tailored architectures with patterned pores often exhibit counterintuitive mechanical behavior, and possess distinct physical and mechanical properties. As one of the recent progresses in this field, soft cellular structures made of hyper-elastic materials with well-designed periodic holes have received increasingly research interests due to their recoverable pattern transformation capability [4]. As reported by several research works, due to their revisable buckling patterns and auxetic responses, soft cellular structures had shown great potentials in many engineering applications, e.g., flexible actuators [5], mechanical assemblies of complex structures [6, 7], tunable phononics [8] and etc.

Designing soft cellular structures with a tailored configuration of pores patterns in inter-pore ligaments to regulate the stiffness distribution and achieve desired responses is currently a very interesting topic in this field. The compaction pattern transformation of rectangle elastomer sheets with uniformly distributed circular or elliptical holes with a specific center-to-center spacing was firstly studied by Mullin *et al.* [4]. Bertoldi *et al.* carried out a series of research works to systematically study the bucking mechanics of cellular structures using different numerical modelling strategies [9], considering negative Poisson's ratio [10] and the effect of the pore shapes [11, 12]. Inspired by the tessellation of a 2D Euclidean plane, Shim *et al.* [13] proposed and studied three new types of soft porous structures with periodic patterns of uniformly distributed circular holes. Florijn *et al.* [14] proposed a novel soft bipolar structures by patterning a regular array of holes with two different sizes in an elastic slab, which allows the polarization direction can be switched. He *et al.* [15] and Li *et al.* [16] attempted to modify the stiffness distribution of the regular soft periodic structures using composite materials. Zhang *et al.* [17, 18] proposed a design of soft cellular metamaterials with periodically distributed orthogonally oriented elliptical holes with dual sizes, which can produce ordered localized deformation under compression. The topology optimization method was employed recently by Dalklint *et al.* [8] to design pores patterns of soft cellular structures to achieve target mechanical properties.

The compacting process and the associated buckling and post-buckling behavior of soft cellular structures are considered as the main factors that affect the structural performance regulation. Extensively experimental [9-13, 19], numerical [9-13, 20] and theoretical studies and works [21-23] on the buckling and post-buckling behavior of planar periodic structures with finite or infinite dimensions have been performed. The novel external actions including multi-physics stimulations [24-26] and multi-axis loading strategies [27, 28] were developed to control the recoverable compactions and the nonlinear instabilities of soft periodic structures. Moreover, many research works in literature have taken advantages of the reversible compacting pattern transformation of 2D soft pores structures to manage its acoustic properties in a tunable and controllable manner [29-35].

Almost all the previous research works on soft cellular structures focused on designing flexible metamaterials with uniform and periodic pore patterns and devoted to study the mechanical properties associated with their global compacting processes. On the other hand, many natural materials and tissues, such as horse hoof wall [36,37] and antler [38], spontaneously form gradient rather than uniform cellular structures that possess optimal mechanical properties. Therefore, applying gradient porosity to tailor mechanical performance of regular cellular structures including metal foam [39-41], original or auxetic honeycombs [42-45], 3D printed lattices [46-51], have been attracted wide research interests for many engineering applications [52-57]. The naturally selected gradient pores of some live tissues and different kinds of designed gradient cellular materials imply that gradient cellular structures could have superior mechanical properties compared with periodic ones. Thereby, in this paper, a novel kind of soft cellular

structures with layer-wisely designed gradient pores is proposed. The unique progressive compacting processes of the gradient soft cellular structures with different porosities and different layer-wise patterns under uniaxial compression and the related mechanical performance including the buckling and post-buckling behaviour, the effect of negative Poisson's ratio are investigated experimentally and numerically.

Thereby, the design methods of soft cellular structures with Unidirectional Layered Gradient Porosity (ULGP) and soft cellular structures with Radial Layered Gradient Porosity (RLGP) are proposed in this paper. Further, a uniaxial compression test is conducted to reveal the progressive compacting processes. Finally, numerical simulations were carried out to investigate the mechanical properties of the designed gradient soft cellular structures, which include the maximum value of nominal Poisson's ratio, average value of nominal Poisson's ratio and nominal elastic modulus.

2. Methodology

Inspired by the microstructural forms of horse hoof wall and antler, a design concept that allows the porosity gradients to vary along each layer is introduced to 2D soft periodic cellular structures, as shown in Figure 1 and Figure 2. The design method that enables cellular structures to possess layer-wisely gradient porosity is proposed and discussed in this section. Furthermore, soft cellular structures with ULGP (Unidirectional Layered Gradient Porosity) and soft cellular structures with RLGP (Radial Layered Gradient Porosity) are designed and studied in this section.

Along the thickness direction of the horse hoof wall, there is an obvious tubular microstructure density gradient from the inner layer to the outer layer, as shown in Figure 1(a) and Figure 1(b). The inner tubular density of the hoof wall is loose, while the outer tubular structure is distributed tightly. Inspired by this microstructural form in nature, we designed soft cellular structures with ULGP that have a large porosity in the top area and a small porosity in the bottom area, as shown in Figure 1(c).

Figure 2(a) illustrates that antlers contain a core of cancellous bone surrounded by compact bone, exhibiting a hierarchical structure. Inspired by the structural form of antlers, soft cellular structures with RLGP that have a large porosity in the central area and a small porosity in surrounding areas are designed, as shown in Figure 2(b).

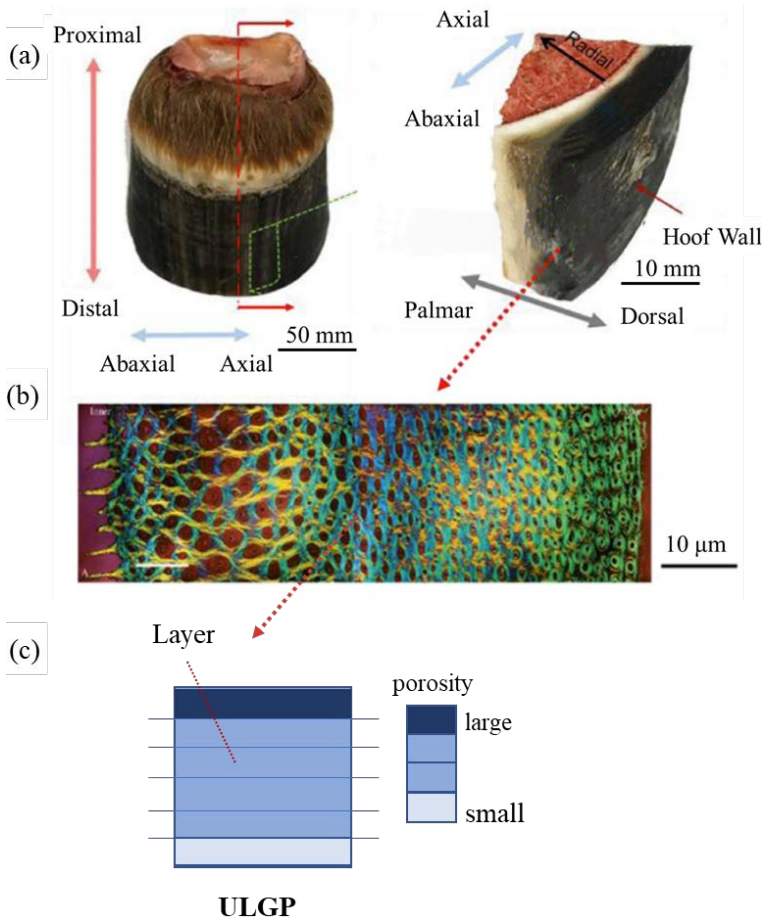

Figure 1 The constructive process of soft cellular structures with ULGP inspired by horse hoof wall (a) Naturally occurring horse hoof (Figure adapted from [36]) (b) A pixilated image of a thick hoof wall sample (Figure adapted from [37]) (c) Soft cellular structures with ULGP

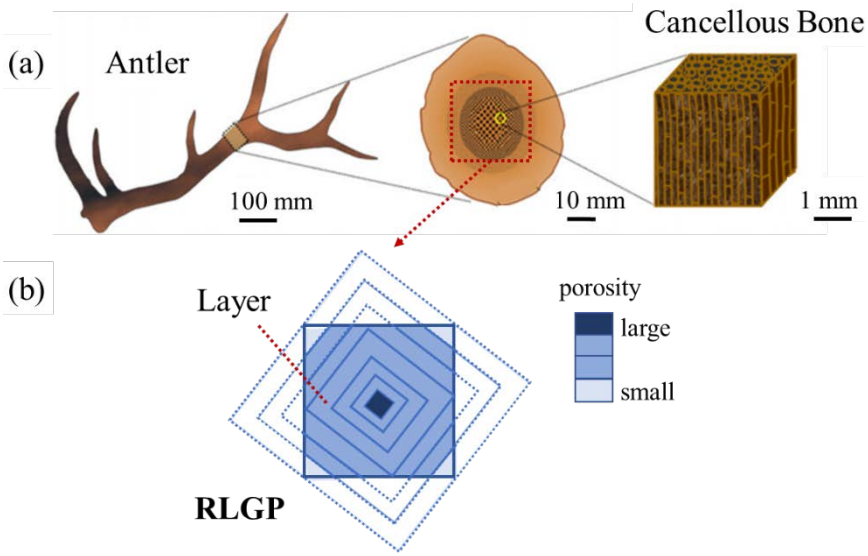

Figure 2 The constructive process of soft cellular structures with RLGP inspired by antler (a) Hierarchical structure of antler (Figure adapted from [38]) (b) Soft cellular structures with RLGP

2.1 Soft cellular structures with ULGP

The design of soft cellular structures with ULGP is carried out in this section, for which soft cellular structures with a periodic cellular pattern along horizontal direction and a gradient varying of porosity along vertical direction is proposed and designed, as shown in Figure 3. Two different distributions for the gradient porosity of soft cellular structures are considered in the design process. One is that the porosity between the layers follows an arithmetic progression pattern, and for the other one, the porosity between the layers is varying in a geometric progression. To avoid out-of-plane buckling deformations during uniaxial compression, large thicknesses are assigned to the design of cellular structures in this work. Eq. (1) gives the mathematical expressions to compute the porosity of each layer, which are derived based on a square representative cell containing a single hole, as shown in Figure 3.

$$\varphi_{ui} = \frac{n_{ui}\pi R_{ui}^2}{D_u W_u} = \frac{n_{ui}\pi R_{ui}^2}{n_{ui} D_u^2} = \frac{\pi R_{ui}^2}{D_u^2} (i = 1, 2, \cdots, n) \tag{1}$$

where φ_{ui} is the original porosity of *i-th* layer of the soft cellular structures with ULGP, R_{ui} is the radius of the hole in *i-th* layer, W_u is the original width of the structures, D_u is the width(height) of square unit cell, and indicates the original height of each layer, n_{ui} is the number of holes in *i-th* layer.

Eq. (2) defines the relationship between the porosity of each layer and the overall porosity of the structures.

$$\varphi_u = \frac{S_u}{W_u H_u} = \frac{n_{u1}\pi R_{u1}^2 + n_{un}\pi R_{un}^2 + \pi \sum_{i=2}^{n-1} n_{ui} R_{ui}^2}{W_u H_u} \tag{2}$$

where φ_u is the original porosity of the whole structure, S_u is the total area of the holes, H_u is the original height of the structure.

Eq. (3) and Eq. (4) define the relationship between the porosity of *i-th* layer and the porosity of the first layer.

$$\varphi_{ui} = \varphi_{u1} + (i-1) d_u \tag{3}$$

$$\varphi_{ui} = q_u^{(i-1)} \varphi_{u1} \tag{4}$$

where d_u is the common difference, q_u is the common ratio.

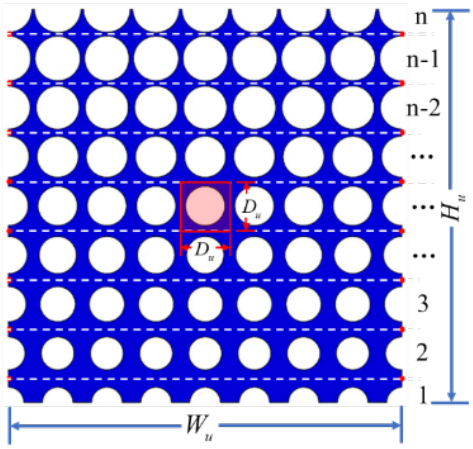

Figure 3 Schematic diagram of the soft cellular structures with ULGP

2.2 Soft cellular structures with RLGP

The design of soft cellular structures with RLGP is carried out in this section. Similar with the

ULGP design, large thicknesses for structures with RLGP are designed to avoid out-of-plane buckling deformations during uniaxial compression. Eq. (5) gives the mathematical expressions for the calculation of porosity of each layer, which are based on a square representative cell containing a single hole as shown in Figure 4.

$$\varphi_{ri} = \frac{n_{ri}\pi R_{ri}^2}{n_{ri}D_r^2} = \frac{\pi R_{ri}^2}{D_r^2}\left(i = 1,2,\cdots,n\right) \tag{5}$$

where φ_{ri} is the original porosity of *i-th* layer of the soft cellular structures with RLGP, R_{ri} is the radius of the hole in *i-th* layer, D_r is the width(height) of square unit cell, and also indicates the original thickness of each layer, n_{ri} is the number of holes in the *i-th* layer.

Eq. (6) defines the relationship between the porosity of the layers.

$$\varphi_{ri} = \varphi_{r1} + (i-1)d_r \tag{6}$$

where d_r is the common difference.

Eq. (7) defines the relationship between the porosity of each layer and the overall porosity of the cellular structures. In fact, Eq. (7) can be further simplified to give the relationship between the overall porosity and the porosity of the first layer.

$$\varphi_r = \frac{S_r}{W_r H_r} = \frac{\sum_{i=1}^{n} n_{ri}\pi R_{ri}^2}{W_r H_r} = \frac{\sum_{i=1}^{n} n_{ri}\pi R_{ri}^2}{\sum_{i=1}^{n} n_{ri}D_r^2} = \frac{\sum_{i=1}^{n} n_{ri}\varphi_{ri}}{\sum_{i=1}^{n} n_{ri}} = \varphi_{r1} + \frac{\sum_{i=1}^{n}(i-1)n_{ri}d_r}{\sum_{i=1}^{n} n_{ri}} \tag{7}$$

where φ_r is the original porosity of the whole structure, S_r is the total area of the holes, W_r is the original width of the structures, H_r is the original height of the structures.

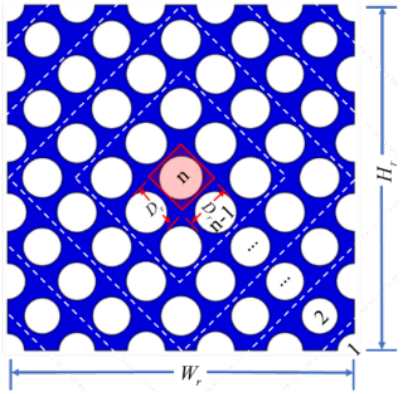

Figure 4 Schematic diagram of the soft cellular structures with RLGP

3. Uniaxial compression test

3.1 Fabrication of the specimens

Two repeated specimens (test specimen and spare specimen) of soft cellular structure with ULGP, which have an initial overall porosity φ_u of 50% and the common difference d_u of 5%, are fabricated and tested in this section. The dimension of the structure $W \times H \times T$ is 80mm × 80mm × 35mm and the hole center distance is 10mm. The process of making the specimen is as follows. Firstly, a mould of the specimen was made of white photosensitive resin materials using 3D printing technology, as shown in Figure 5. Figure 5(a) shows the components of the specimen mould, including a base, side plates, a top plate, and round bars with different diameters. Figure 5(b) and Figure 5(c) show different viewings of the mould after assembly, respectively. Next, silicone rubber (type E625, its density is 1.05g/cm^3) is

poured into the mould. Before the action of pouring, a very thin layer of release agent is applied to the mould to ensure that an intact specimen can be removed from the mould. Finally, the poured silicone rubber specimen is placed in a vacuum machine for 10 minutes and then placed in a room-temperature environment until it is fully cured. The fabricated specimen is shown in Figure 5(d).

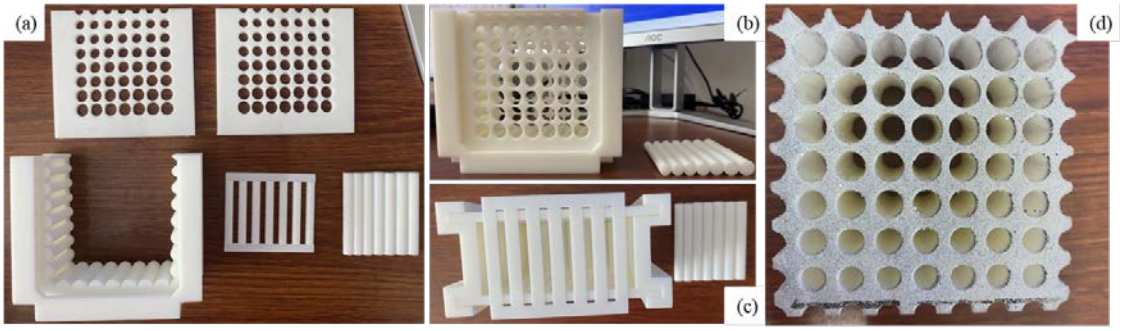

Figure 5 Diagram of the specimen

(a) Components of the specimen mould, including the base, side plates, top plate, and round bars of different diameters (b) Front view of the mould after assembly (c) Top view of the mould after assembly (d) Fabricated specimen

3.2 Experimental procedure

In the uniaxial compression test, the specimen is not clamped to the fixture. Because the horizontal surface of the specimen is not lubricated, there is enough friction between the specimen and the fixture to ensure that no relative motion occurs between the top and bottom surfaces of the specimen. The experimental equipment is shown in Figure 6, and a displacement with a loading rate of 6 mm/min and a loading period of 4 min is applied for the experimental test. The deformation of the specimen was monitored using a non-contact 3D full-field strain measurement system with a high-speed camera, as shown in Figure 6(b). The high-speed camera is taking pictures at one-second intervals with a nominal strain increment of $\Delta\varepsilon$=0.00125. A nominal stress σ is obtained by dividing the experimentally obtained force with the area of the bottom surface of the specimen. The displacement is divided by the initial height of the specimen to give a nominal strain ε. The maximum value of the nominal Poisson's ratio ν_{max} is defined as the maximum horizontal strain divided by the negative value of the vertical strain.

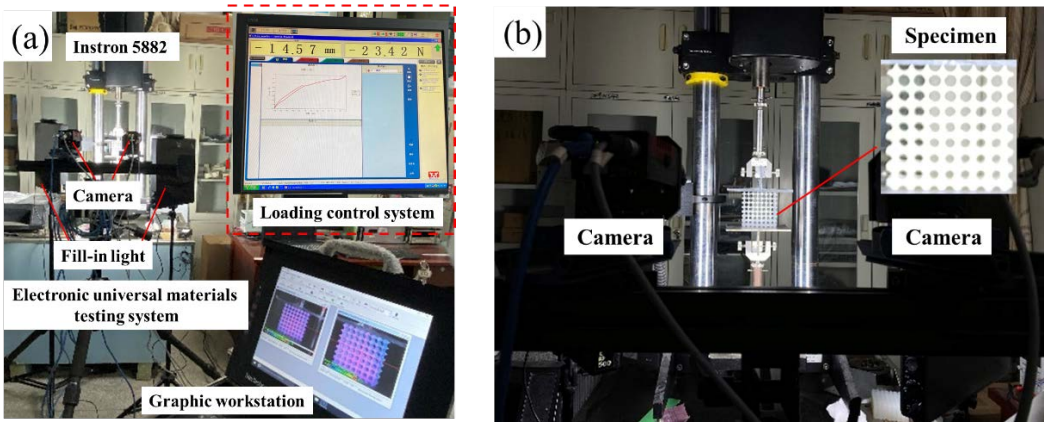

Figure 6 Diagram of experimental equipment

(a) The experimental equipment layout (b) The experimental loading equipment

3.3 Experimental results and discussion

The deformation behavior of soft cellular structures with ULGP under uniaxial compression undergoes three phases, i.e., the linear elastic phase, the stress plateau phase, and the densification phase. If applying the ABAQUS/Standard for the numerical analysis, the deformation behavior of soft cellular structures in the densification phase cannot be captured accurately due to the mesh distortion issue at high strains. Therefore, the numerical simulation process was carried out using the dynamic explicit (ABAQUS/Explicit) step, which can lead to convergent and accurate numerical results to this problem. To study the effect of the overall porosity and the gradient of porosity of each layer on the buckling and post-buckling behavior of 2D soft cellular structures, finite element models with different geometrical parameters were established. To this end, a Python program was written to automatically generate ABAQUS finite element models with respect to different geometrical parameters (see Supplemental Material for details on the finite element simulations). Nominal stresses σ and nominal strains ε are calculated in the same way with the method shown in Figure S2.

As can be seen from the relationship denoted by the nominal stress-strain curves shown in Figure 7, the experimental results agree well with the numerical simulation results when the nominal strain is small. The blue, green, and purple areas of the diagram correspond to the linear elastic phase, stress plateau phase, and densification phase, respectively. At the nominal strain ε=-0.0375, a clear stress plateau appears in the numerical simulation (σ =-0.0098) and the experimental nominal stress shows a smooth increase. When the nominal strain reaches ε=-0.145, the soft cellular structure enters the densification phase, and the nominal stress increases sharply. The high porosity areas of cellular structures are densified first. After the cellular structures are densified, the edges of the holes touch each other, which increases the stiffness and load-carrying capacity of the structures. Next, the areas with low porosity begin to densify due to the stiffness of these areas is less than that of areas that have be compacted. Cellular structures exhibit obviously progressive compaction deformation behavior. Differences between the numerical simulation results and the experimental results are mainly given rise by manufacturing defects.

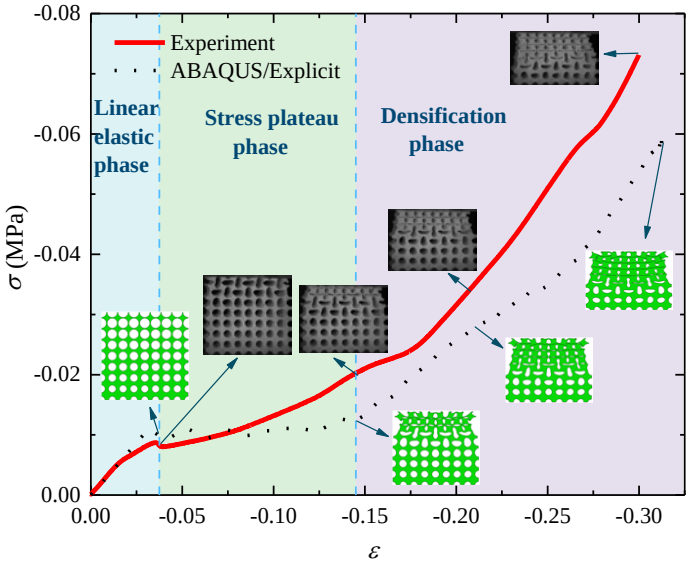

Figure 7 Curves of nominal stress-strain for experiment and numerical simulation

The curves shown in Figure 8 denote the relationship of the maximum value of nominal Poisson's ratio versus the nominal strain of soft cellular structure. Figure 8 illustrates that the simulation results follow the same trend as the experimental results. However, the values of the two curves are deviated

significantly. This may be due to the manufacturing defects in the experimental specimen. Failure to ensure ideal temperature conditions during the fabrication of the specimens may affect the elimination of air bubbles during the solidification of the specimens. The ligaments between the holes in the specimens are very thin and manufacturing defects can significantly affect the mechanical properties of the specimens.

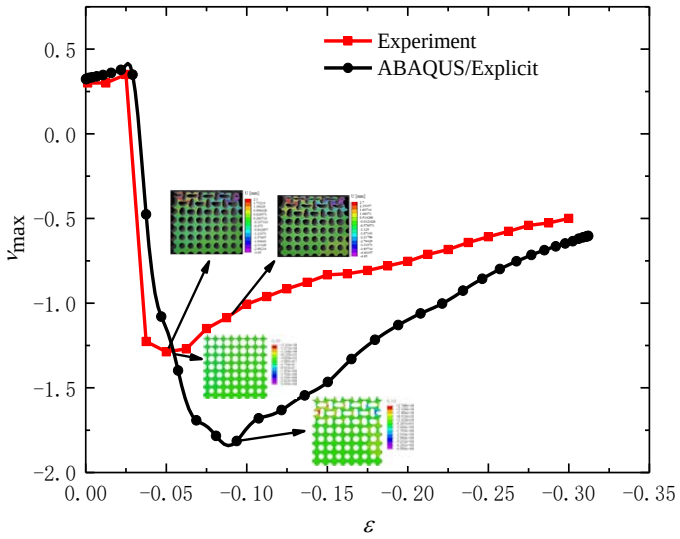

Figure 8 Curves of the maximum value of nominal Poisson's ratio versus nominal strain for soft cellular structure for experiment and numerical simulation

Table 1 shows the nominal principal strains of the cellular structures at different nominal strains obtained from the experimental testing. Table 1 shows the nominal principal strains of the cellular structures at different nominal strains given by the numerical simulation. In comparison, the nominal principal strains obtained from the experimental testing and that predicted by the numerical simulations are in excellent agreement. Areas with large porosity are deformed in buckling first and areas of low porosity are deformed later, producing a progressive compaction progress. However, during the experiment, the electronic universal testing machine indenter and the upper surface of the specimen are not guaranteed to be in full contact at the same time. Therefore, the right half of the specimen contacts first at a smaller nominal strain, resulting in a larger deformation. However, it has less influence on the auxetic behavior of the soft cellular structures.

Table 1 Contour of	Experiment	Numerical simulation
0.1	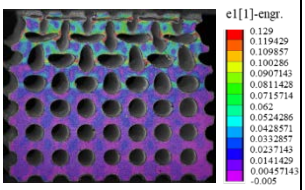	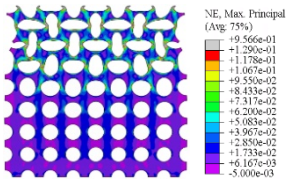
0.2	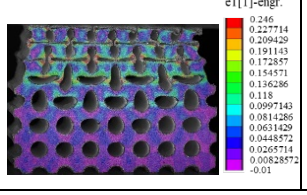	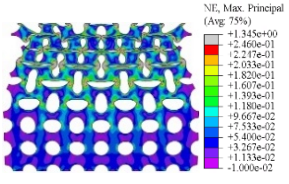

0.3	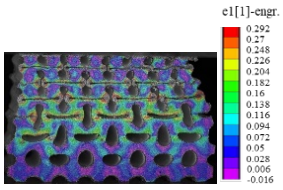	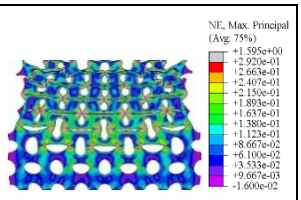

4. Results and discussion

4.1 In-plane eigenvalue buckling analysis

Figure 9 illustrates the first order buckling mode of soft cellular structures with ULGP with an overall porosity of φ_u=50%. In Figure 9(a), when the circular holes are arranged in a periodic pattern, the inter-hole ligaments are rotated due to the elastic instability under axial compression. The periodic porous structures exhibit an overall buckling deformation behaviour, and the circular holes become mutually orthogonal elliptical holes. With increasing common difference, the difference of porosity between the top and bottom edges of the structure reaches 40%, as shown in Figure 9(f). In this case, the upper area with the large porosity showed mutually orthogonal elliptical holes. It means that the structures exhibit local buckling behaviour. (The red rectangle marks the area where the buckling deformation occurs.)

Table 2 demonstrates the critical strain of soft cellular structures with ULGP with an overall porosity of φ_u=50%. When the common difference is 0, the structure exhibits an overall buckling behavior with a critical strain of 0.0609. As the common difference increases, the critical strain decreases. When the common difference is 5%, the structure exhibits local buckling behavior and the critical strain reduces to 0.0231. This is because the overall porosity of the structure is constant and the larger the variation between the porosities of the layers, the area of large porosity is weak and more easily subject to buckling deformation. The critical displacement load of cellular structures with ULGP with common difference of 5% is greatly smaller than that of the periodic cellular structures, which provides the potential to achieve high sensitivity of the tactile sensors.

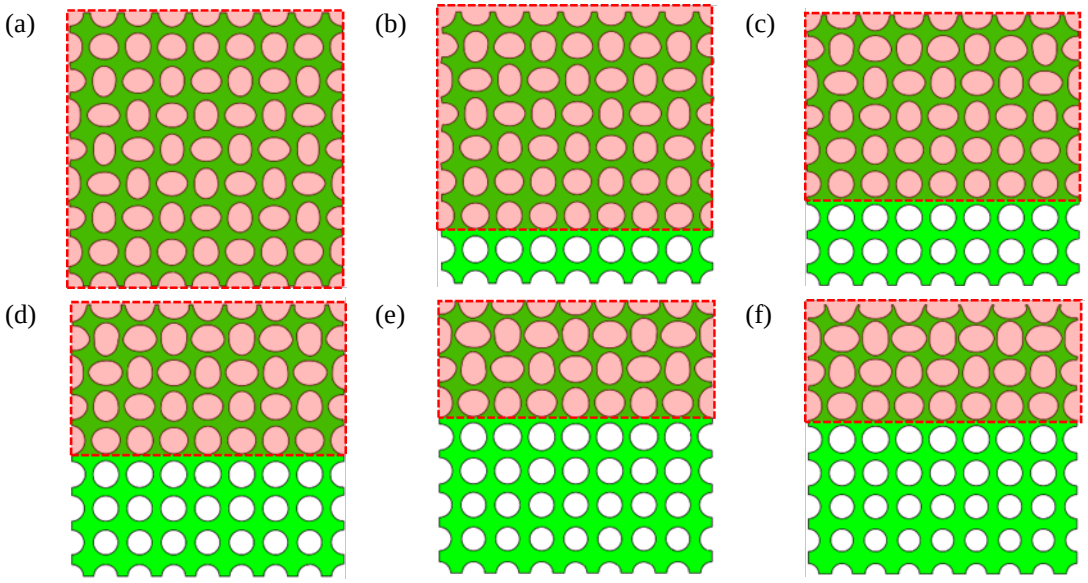

Figure 9 The first-order buckling model of soft cellular structures with ULGP (φ_u=50%)
(a) d_u=0 (b) d_u=1% (c) d_u=2% (d) d_u=3% (e) d_u=4% (f) d_u=5%

Table 2 Critical strain of soft cellular structures with ULGP (φ_u=50%)

d_u	0	1%	2%	3%	4%	5%
Critical strain	0.0609	0.0571	0.0495	0.0413	0.0326	0.0231

4.2 Post-buckling analysis

In this section, firstly, the effect of gradient variation of porosity on the maximum value of nominal Poisson's ratio and the average value of nominal Poisson's ratio of cellular structures are studied and discussed. Secondly, the effect of gradient variation of porosity on the critical buckling load is investigated. Finally, the effect of gradient variation of porosity on the nominal elastic modulus is analyzed. As given by Eq. (8), the maximum value of the nominal Poisson's ratio is defined as the maximum horizontal strain divided by the negative value of the vertical strain. As the cellular structures are square, the maximum value of the nominal Poisson's ratio is determined by dividing the maximum horizontal displacement by the negative value of the vertical displacement. It is to be noted that the maximum horizontal displacement is the absolute maximum value. The average value of the nominal Poisson's ratio is defined as the average horizontal strain divided by the negative value of the vertical strain, as given by Eq. (9). Similarly, the average value of the nominal Poisson's ratio is calculated by dividing the average horizontal displacement with the negative value of the vertical displacement. A Python program is used to extract the horizontal displacement of each node on both left and right sides of the structure. The average horizontal displacement is the average of the horizontal displacements of all nodes. Nominal elastic modulus is obtained by calculating the slope of the nominal stress-strain curve during the linear elastic phase.

$$\nu_{\max} = -\frac{\varepsilon_{x,\max}}{\varepsilon_y} = -\frac{\Delta_{x,\max}/W}{\Delta_y/H} = -\frac{\Delta_{x,\max}}{\Delta_y} \tag{8}$$

$$\overline{\nu} = -\frac{\overline{\varepsilon}_x}{\varepsilon_y} = -\frac{\overline{\Delta}_x/W}{\Delta_y/H} = -\frac{\overline{\Delta}_x}{\Delta_y} \tag{9}$$

4.2.1 Maximum value of the nominal Poisson's ratio

Figure 10 and Figure 11 illustrate the maximum value of nominal Poisson's ratio versus nominal strain of soft cellular structures with ULGP, for which the porosity gradients between the layers are varying in an arithmetic progression and in a geometric progression respectively. It was found that the cellular structures with large overall porosity exhibit a small initial maximum value of nominal Poisson's ratio. It is also interestingly to note that they exhibit an obvious large value of negative Poisson's ratio effect. In Figure 10(a), when the nominal strain of ε=-0.165, the curve of the maximum value of nominal Poisson's ratio versus nominal strain with the common difference of d_u=5% starts to decrease significantly. Finally, the maximum value of the nominal Poisson's ratio drops to -0.21. This change is due to the side-bending deformation of the structure. In contrary, the periodic soft cellular structure with an overall porosity of φ_u=20% showed macroscopic instability along the loading path.

Figure 10(d) shows that a larger common difference d_u leads to an earlier appearance and a larger absolute value of the negative Poisson's ratio effect for the cellular structures under uniaxial compression. It is surprisingly noted that, after the maximum value of the nominal Poisson's ratio reaches a minimum, the curves begin to rise. This is because a larger common difference d_u leads to a more unequal distribution of structural stiffness, and higher porosity areas will be more easily to lose its stability in the densification phase. After the densification of high porosity areas, the maximum value of the horizontal

displacement of the structure remains constant, although the vertical displacement gradually increases, the curves of the maximum value of nominal Poisson's ratio versus nominal strain start to rise. Eventually, the horizontal displacement of the periodic cellular structure after densification is approximately the same with that of the gradient cellular structure, so the curves of the maximum value of nominal Poisson's ratio versus nominal strain eventually converge. In short, the periodic cellular structure exhibits a uniform compaction behavior, whereas the gradient cellular structure shows a progressive compaction behavior. The gradient cellular structures with progressive compaction behaviour can enable tactile sensors to achieve high sensitivity in a wider pressure range than usual.

Similar with the results shown in Figure 10, cellular structures with large overall porosity show a small initial maximum value of nominal Poisson's ratio yet exhibit an obvious large value of negative Poisson's ratio effect as shown in Figure 11. The difference is that the soft cellular structures with ULGP do not appear a negative Poisson's ratio effect, when the overall porosity of φ_u=20%. This is because the macroscopic instability of the structures along the loading path is likely to occur for the cellular structures with a small variation of porosity between the layers, i.e., the periodic cellular structures. Figure 11(d) shows that a larger common ratio q_u leads to an earlier appearance and a larger absolute value of the negative Poisson's ratio effect for the cellular structures, which are under uniaxial compression.

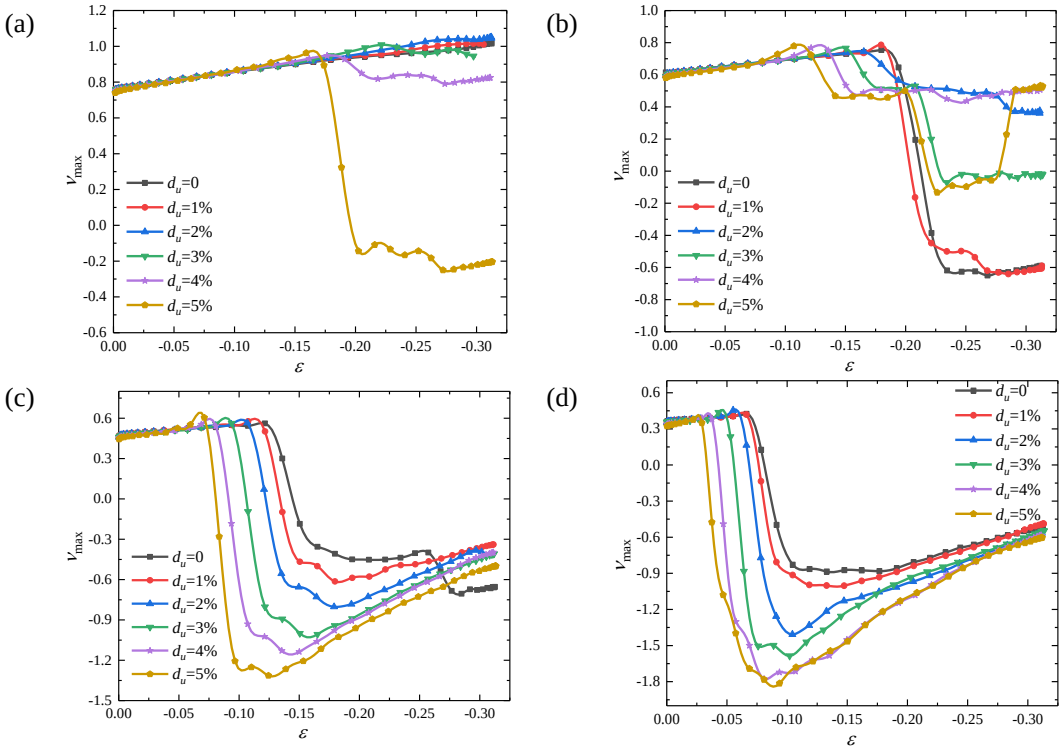

Figure 10 Curves of the maximum value of nominal Poisson's ratio versus nominal strain of soft cellular structures with ULGP in an arithmetic progression

(a) φ_u=20% (b) φ_u=30% (c) φ_u=40% (d) φ_u=50%

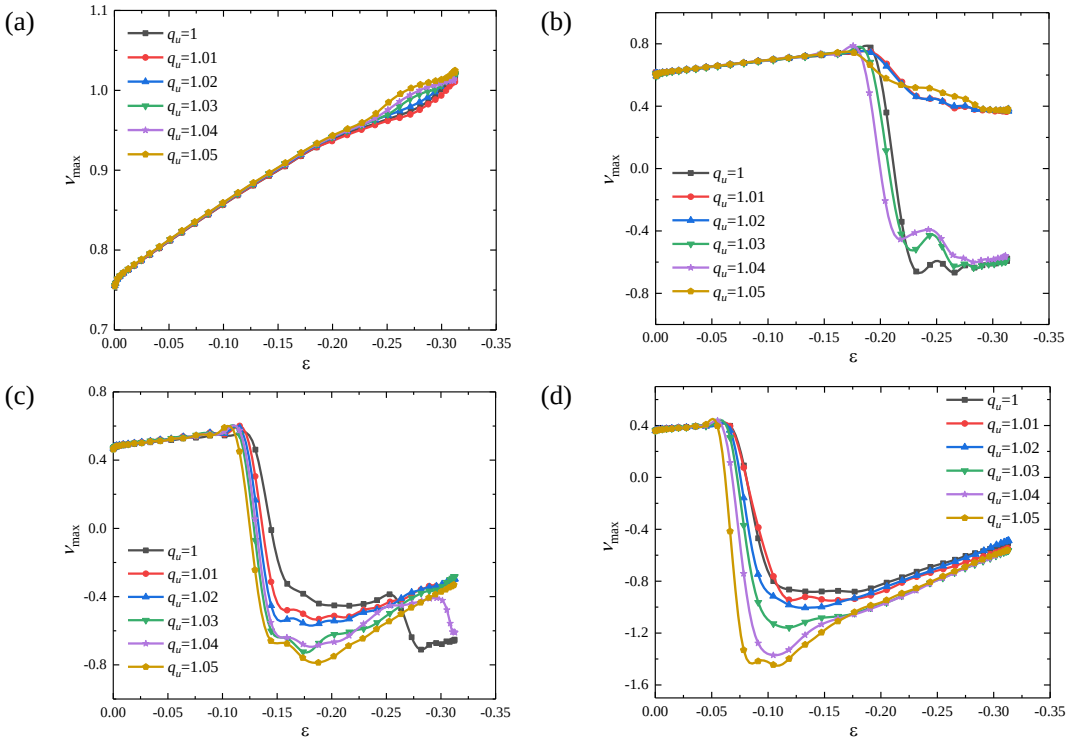

Figure 11 Curves of the maximum value of nominal Poisson's ratio versus nominal strain of soft cellular structures with ULGP in a geometric progression
(a) φ_u=20% (b) φ_u=30% (c) φ_u=40% (d) φ_u=50%

Figure 12 shows the maximum value of nominal Poisson's ratio distribution of soft cellular structures with ULGP, for which the porosity gradients between the layers are varying in an arithmetic progression. The shades of colors in the diagram indicate that the maximum value of the nominal Poisson's ratio is in different ranges. As shown in Figure 12(a), the cellular structures in the bottom-left region do not appear the negative Poisson's ratio effect. The maximum value of the nominal Poisson's ratio of the cellular structures in the upper right region is smaller than -1. This means that the maximum value of nominal Poisson's ratio is not only closely related to the overall porosity of the structures, but also related to the value of the common difference d_u. Different with the results shown in Figure 12(a), the cellular structures in the left region do not appear the negative Poisson's ratio effect as shown in Figure 12(b). The maximum value of the nominal Poisson's ratio of the cellular structures in the right region is smaller than -1. When the overall porosity is 30%, the maximum value of the nominal Poisson's ratio is sometimes positive and sometimes negative. This means that cellular structures with an overall porosity of 30% is in a critical state of stability.

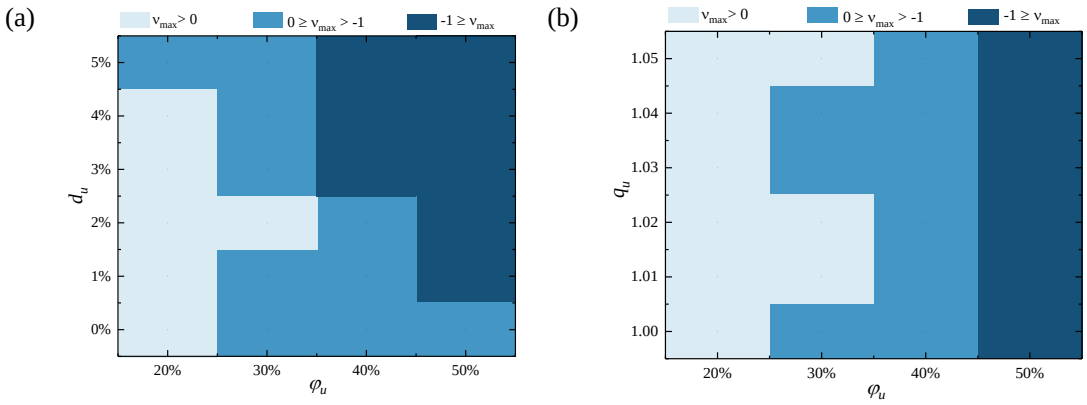

Figure 12 Schematic diagram of the maximum value of the nominal Poisson's ratio distribution of soft cellular structures with ULGP

(a) in an arithmetic progression (b)in a geometric progression

4.2.2 Average value of the nominal Poisson's ratio

Figure 13 illustrates the average value of nominal Poisson's ratio versus nominal strain of soft cellular structures with ULGP, for which the porosity gradients between the layers are varying in an arithmetic progression. It was observed that cellular structures with large overall porosity show a smaller initial average value of nominal Poisson's ratio. In Figure 13(a), structures with common differences of d_u = 3%, 4%, 5% experience the side-bending deformation and result in a significant drop in the curve.

In Figure 13(d), the larger the common difference d_u, the more unequal the stiffness distribution of the cellular structures is and the earlier the negative Poisson's ratio effect appears during uniaxial compression. Unlike Figure 10(d), the absolute value of the final negative Poisson's ratio decreases as the common difference increases. This is because that the areas of the structure with high porosity are compacted and the horizontal displacement reaches a maximum value. At this time the areas of small porosity are not compacted, and the horizontal displacement is small. The uncompacted area increases with the growth of common differences, which results in a smaller average value of horizontal displacement. The tendency of the curves reflects the gradient cellular structures producing progressive compaction deformation behavior under uniaxial compression.

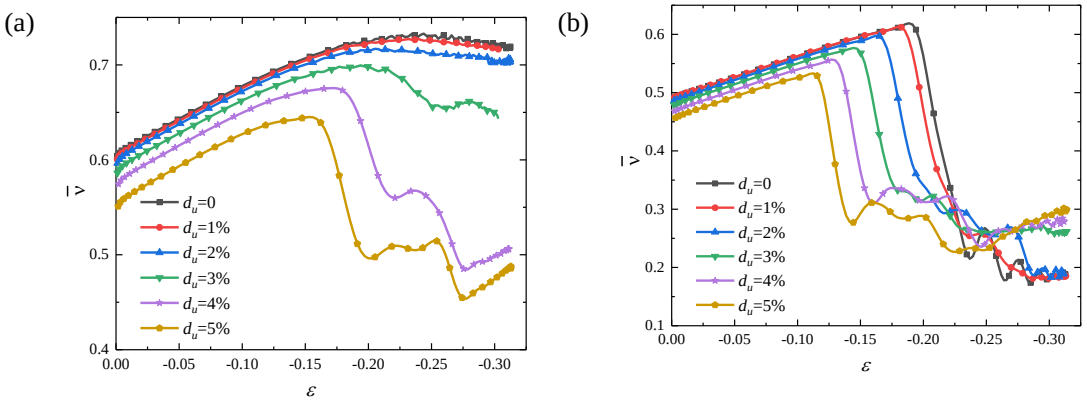

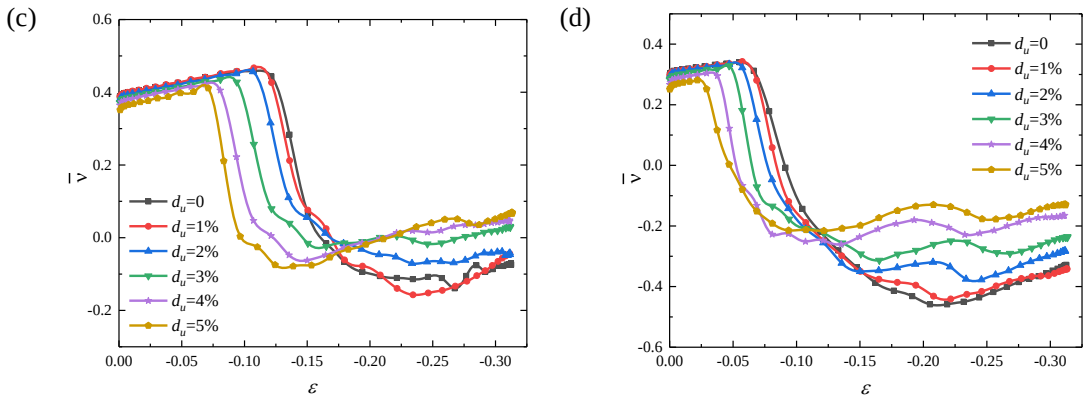

Figure 13 Curves of the average value of nominal Poisson's ratio versus nominal strain of soft cellular structures with ULGP in an arithmetic progression
(a) φ_u=20% (b) φ_u=30% (c) φ_u=40% (d) φ_u=50%

4.2.3 Nominal elastic modulus

Figure 14 illustrates the nominal stress versus nominal strain of soft cellular structures with ULGP, in which the porosity gradient variations between the layers follow the arithmetic progression. It was found that cellular structures with larger overall porosity have lower overall stiffness and exhibit smaller plateau stresses. In Figure 14(a), the stress plateau starts to appear in the curve of nominal stress versus nominal strain with a common difference of d_u=5% when the nominal strain of ε=-0.165. As the compression displacement increases up to16mm, the areas of the structures with high porosity enter the densification phase and the curves exhibit a distinct rising tendency. In contrast, for the periodic soft cellular structure with an overall porosity of φ_u=20%, the macroscopic instability occurs along the loading path resulting in no apparent stress plateau.

It was observed that structures with the same overall porosity have the same nominal elastic modulus. This indicates that the nominal elastic modulus of the structures highly depends on the overall porosity. When the overall porosity is the same for the structures, the larger the common difference d_u is, it is easier for the cellular structures to develop a stress plateau under uniaxial compression. This is because when the overall stiffness remains almost constant, a larger common difference d_u leads to a more unequal distribution of the structural stiffness. Areas of cellular structures with high porosity have low stiffness, which therefore are very easy to buckle with low plateau stress. It is interestingly to note that the soft cellular structures with larger common difference d_u, the curve of nominal stress versus nominal strain will sharply raise during the densification phase.

Figure 15 illustrates the nominal stress versus nominal strain for soft cellular structures with RLGP, in which different porosity gradients between the layers are varying with an arithmetic progression. It was observed that no obvious nominal plateau stress is observed, which means that the structures are in the linear elastic phase. With the increase of the overall porosity, the structural stiffness decreases. Furthermore, when the overall porosity of the structure remains constant, the overall stiffness of cellular structures with RLGP shows an increasing trend compared with that of the periodic cellular structures, which have the magnitude of variation in porosity of each layer. The small porosity of the outer area of soft cellular structures with RLGP corresponds to a hard shell surrounding an area of large porosity. When uniaxial compressive loads are applied, the internal areas are the first to exhibit local buckling behaviour. However, the external areas restrain the deformation of the internal areas, resulting in structures with a larger nominal modulus of elasticity than periodic cellular structures.

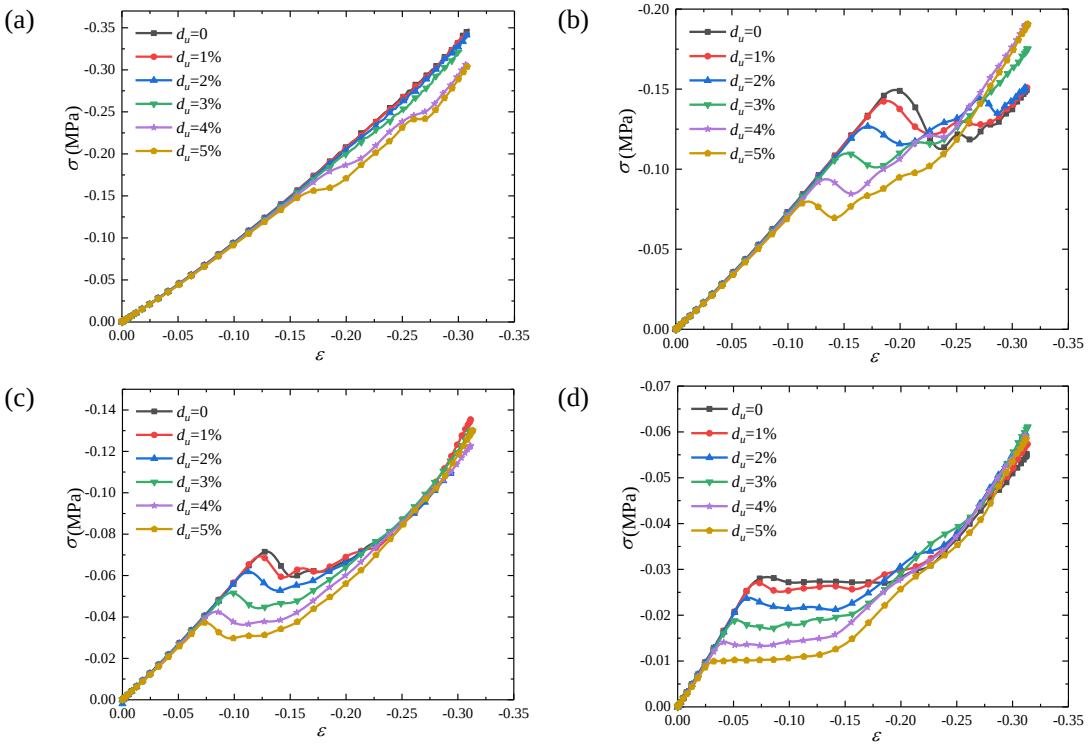

Figure 14 Curves of nominal stress versus nominal strain of soft cellular structures with ULGP in an arithmetic progression

(a) φ_u=20% (b) φ_u=30% (c) φ_u=40% (d) φ_u=50%

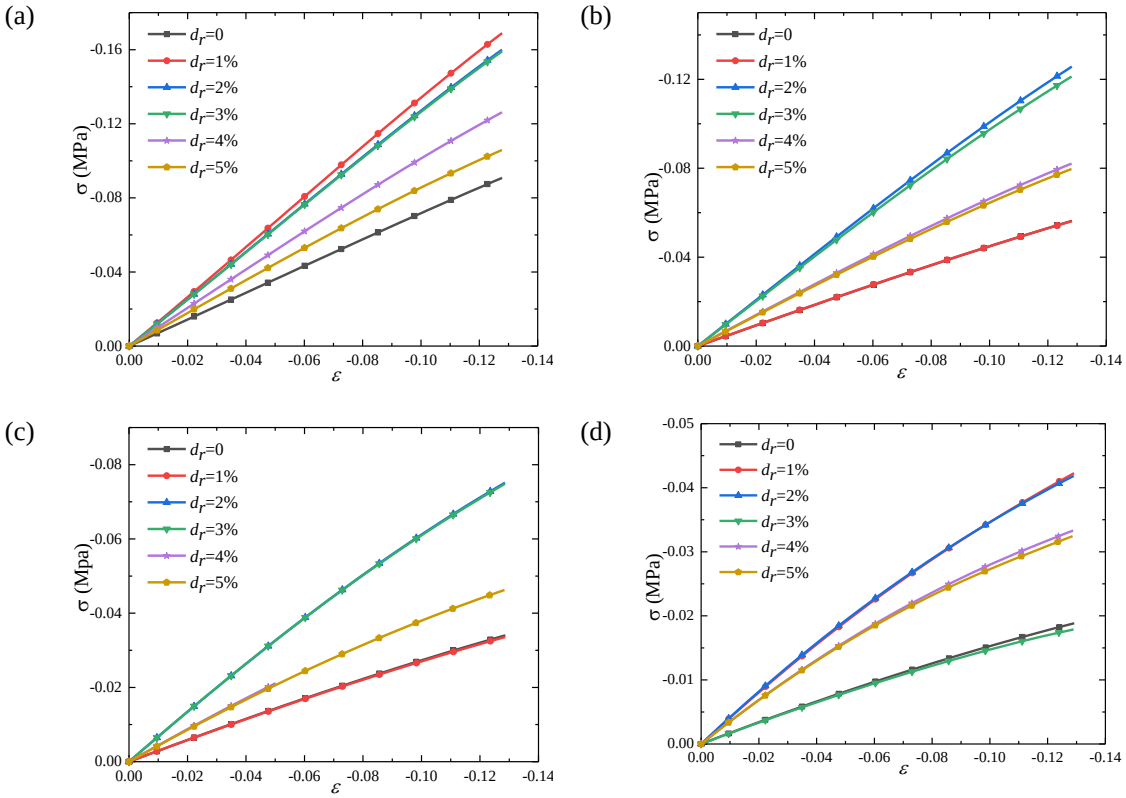

(e)

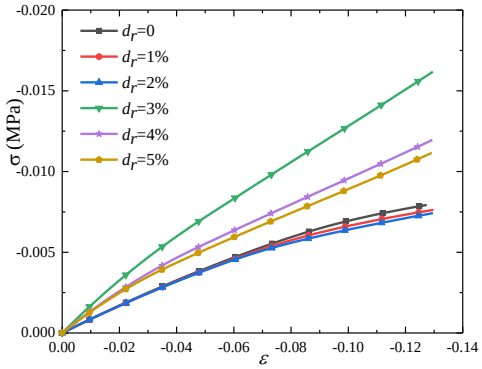

Figure 15 Curves of nominal stress versus nominal strain of soft cellular structures with RLGP in an arithmetic progression

(a) φ_r=20% (b) φ_r=30% (c) φ_r=40% (d) φ_r=50% (e) φ_r=60%

5 Conclusions

This study proposed and designed a kind of novel soft cellular structures with layer-wisely gradient porosity, which exhibit a distinct progressive compaction behavior. The mechanical properties of the designed structures under uniaxial compression are analyzed by experiments and finite element simulations. The following conclusive points were drawn from our study:

Firstly, when the overall porosity of 2D soft cellular structures with ULGP is small, macroscopic instability occurs along the loading path resulting in no negative Poisson's ratio effect. With the increase of the overall porosity of the structure, a negative Poisson's ratio effect caused by mechanical instability appears.

Secondly, when the overall porosity of the structure remains a constant, due to the progressive compaction deformation behavior of the soft cellular structures with ULGP, the maximum value of the nominal Poisson's ratio shows a different increasing tendency compared with that of the periodic cellular structures. The maximum absolute values of negative Poisson's ratio of current gradient soft cellular structures is 2.113 time than that of periodic ones with a same overall porosity.

Thirdly, the maximum value of the nominal Poisson's ratio not only highly depends on the overall porosity of the structures, but also the variation of porosity between the layers. This novel finding greatly expands the design space for 2D soft cellular structures with negative Poisson's ratios.

Finally, when the overall porosity of the structure remains a constant, the nominal elastic modulus of the soft cellular structures with RLGP is significantly higher than that of the periodic cellular structures. The nominal elastic modulus of the gradient structure can be increased by 124.3% compared to a periodic structure with a same overall porosity. This indicates that the stiffness of soft cellular structures with RLGP is larger and provides a wider scope for applications than the other types of soft cellular structures.

Applying gradient porosity for soft cellular structures largely expands the design freedom, which enables the design of soft cellular structures with superior mechanical properties for many potential applications. For example, tactile sensors that are implemented using soft cellular structures with gradient porosity can response a wide pressure range. When metallic materials are employed to fabricate gradient cellular structures, superior impact-resistance structures with high energy absorption performance can be achieved. This is because the nominal elastic modulus of gradient cellular structures is greater than that of periodic ones with a same porosity, as such, more energy can be absorbed per unit volume of gradient cellular structures when the same plastic deformation is produced. However, the present study focuses on variations of deformation behaviour and mechanical properties of the gradient cellular structures.

Energy absorption and elastic wave band gap of these structures should be systematically investigated in the future.

Acknowledgements

We thank the supporting from the National Natural Science Foundation of China (12002247), the Natural Science Foundation of Hubei Province (2018CFB129), the Fundamental Research Funds for the Central Universities of China (WUT: 2016IVA022 and WUT: 2021IVB013) and the National innovation and entrepreneurship training program for college students of China (202110497065).

Reference

[1] Gibson LJ, Ashby MF. Cellular solids: structure and properties. Cambridge University Press, 1997.

[2] Lakes R. Foam structures with a negative Poisson's ratio. Science, 1987, 235(4792):1038–1040.

[3] Bluhm GL, Sigmund O, Wang FW, et al. Nonlinear compressive stability of hyperelastic 2D lattices at finite volume fractions. Journal of the Mechanics and Physics of Solids, 2019, 137:103851.

[4] Mullin T, Deschanel S, Bertoldi K, et al. Pattern transformation triggered by deformation. Physical Review Letters, 2007, 99(8):084301.

[5] Yang D, Mosadegh B, Ainla A, et al. Buckling of elastomeric beams enables actuation of soft machines. Advanced Materials, 2015, 27(41):6323-6327.

[6] Zhang Y, Matsumoto EA, Peter A, et al. One-step nanoscale assembly of complex structures via harnessing of elastic instability. Nano Letters, 2008, 8(4):1192-1196.

[7] Zhao HB, Li K, Han MD, et al. Buckling and twisting of advanced materials into morphable 3D mesostructures. Proceedings of the National Academy of Sciences, 2019, 116(27):13239-13248.

[8] Dalklint A, Wallin M, Bertoldi K, et al. Tunable phononic bandgap materials designed via topology optimization. Journal of the Mechanics and Physics of Solids, 2022, 163:104849.

[9] Bertoldi K, Boyce MC, Deschanel, et al. Mechanics of deformation-triggered pattern transformations and superelastic behavior in periodic elastomeric structures. Journal of the Mechanics and Physics of Solids, 2008, 56(8):2642-2668.

[10] Bertoldi K, Reis PM, Willshaw S, et al. Negative Poisson's ratio behavior induced by an elastic instability. Advanced Materials, 2010, 22(3):361-366.

[11] Overvelde JTB, Shan S, Bertoldi K. Compaction through buckling in 2D periodic, soft and porous structures: effect of pore shape. Advanced Materials, 2012, 24(17):2337-2342.

[12] Overvelde JTB, Bertoldi K. Relating pore shape to the non-linear response of periodic elastomeric structures. Journal of the Mechanics and Physics of Solids, 2014, 64:351-366.

[13] Shim J, Shan S, Kosmrlj A, et al. Harnessing instabilities for design of soft reconfigurable auxetic/chiral materials. Soft Matter, 2013, 9(34):8198-8202.

[14] Florijn B, Coulais C, van Hecke M. Programmable mechanical metamaterials. Physical Review Letters, 2014, 113(17):175503.

[15] He YH, Zhou Y, Liu ZS, et al. Pattern transformation of single-material and composite periodic cellular structures. Materials and Design, 2017, 132:375-384.

[16] Li J, Rudykh S. Tunable microstructure transformations and auxetic behavior in 3D-printed multiphase composites: the role of inclusion distribution. Composites Part B, 2019, 172:352-362.

[17] Zhang YF, Li B, Zheng QS, et al. Programmable and robust static topological solitons in mechanical metamaterials. Nature Communications, 2019, 10:5605.

[18] Zhang YF, Wang YJ, Chen CQ. Ordered deformation localization in cellular mechanical metamaterials. Journal of the Mechanics and Physics of Solids, 2019, 123:28-40.

[19] Yang D, Jin L, Martinez RV, et al. Phase-transforming and switchable metamaterials. Extreme Mechanics Letters, 2016, 6:1-9.

[20] Coulais C. Periodic cellular materials with nonlinear elastic homogenized stress-strain response at small strains. International Journal of Solids and Structures, 2016, 97-98:226-238.

[21] Matsumoto EA, Kamien R. Elastic-instability triggered pattern formation. Physical Review E, 2009, 80(2):021604.

[22] Kapko V, Treacy MMJ, Thorpe MF, et al. On the collapse of locally isostatic networks. Proceedings of the Royal Society A, 2009, 465(2111):3517-3530.

[23] Bar-Sinai Y, Librandi G, Bertoldi K, et al. Geometric charges and nonlinear elasticity of two-dimensional elastic metamaterials. Proceedings of the National Academy of Sciences of the United States of America, 2020, 117(19):10195-10202.

[24] Tipton CR, Han E, Mullin T. Magneto-elastic buckling of a soft cellular solid. Soft Matter, 2012, 8(26):6880-6883.

[25] Li J, Shim J, Deng J, et al. Switching periodic membranes via pattern transformation and shape memory effect. Soft Matter, 2012, 8(40):10322-10328.

[26] Li DM, Zhang Z, Liew KM. A numerical framework for two-dimensional large deformation of inhomogeneous swelling of gels using the improved complex variable element-free Galerkin method. Computer Methods in Applied Mechanics and Engineering, 2014, 274: 84-102.

[27] Qiu H, Li Y, Gao TF, et al. Deformation and pattern transformation of porous soft solids under biaxial loading: experiments and simulations. Extreme Mechanics Letters, 2018, 20:81-90.

[28] Li DM, Kong LH, Qian YC. On compacting pattern control of finite-size 2D soft periodic structures through combined loading. Engineering Structures, 2022, 266:114574.

[29] Bertoldi K, Boyce MC. Mechanically triggered transformations of phononic band gaps in periodic elastomeric structures. Physical Review B, 2008, 77(5):052105.

[30] Bertoldi K, Boyce MC. Wave propagation and instabilities in monolithic and periodically structured elastomeric materials undergoing large deformations. Physical Review B, 2008, 78(18):184107.

[31] Wang P, Shim J, Bertoldi K. Effects of geometric and material nonlinearities on tunable band gaps and low-frequency directionality of phononic crystals. Physical Review B, 2013, 88(1):014304.

[32] Shan S, Kang SH, Wang P, et al. Harnessing multiple folding mechanisms in soft periodic structures for tunable control of elastic waves. Advanced Functional Materials, 2014, 24(31):4935-4942.

[33] Shim J, Wang P, Bertoldi K. Harnessing instability-induced pattern transformation to design tunable phononic crystals. International Journal of Solids and Structures, 2015, 58:52-61.

[34] Javid F, Wang P, Shanian A, et al. Architected materials with ultra-low porosity for vibration control. Advanced Materials, 2016, 28(28):5943-5948.

[35] Gao N, Li J, Bao RH, et al. Harnessing uniaxial tension to tune Poisson's ratio and wave propagation in soft porous phononic crystals: an experimental study. Soft Matter, 2019, 15(14):2921-2927.

[36] Huang W, Yaraghi NA, Yang W, et al. A natural energy absorbent polymer composite: the equine hoof wall. Acta Biomaterialia, 2019, 90:267-277.

[37] Kasapi MA, Gosline JM. Design complexity and fracture control in the equine hoof wall. Journal of Experimental Biology, 1997, 200(11):1639-1659.

[38] Chen PY, Lin AYM, Lin YS, et al. Structure and mechanical properties of selected biological materials. Journal of the Mechanical Behavior of Biomedical Materials, 2008, 1(3):208-226.

[39] Brothers AH, Dunand DC. Mechanical properties of a density-graded replicated aluminum foam. Materials Science and Engineering A, 2008, 489(1-2):439-443.

[40] Zhang JJ, Wang ZH, Zhao LM. Dynamic response of functionally graded cellular materials based on the Voronoi model. Composites Part B, 2016, 85:176-187.
[41] Yang ZC, Wu HL, Yang J, et al. Nonlinear forced vibration and dynamic buckling of FG graphene-reinforced porous arches under impulsive loading. Thin-Walled Structures, 2022, 181:110059.
[42] Ajdari A, Nayeb-Hashemi H, Vaziri A. Dynamic crushing and energy absorption of regular, irregular and functionally graded cellular structures. International Journal of Solids and Structures, 2011, 48(3-4):506-516.
[43] Chen D, Kitipornchai S, Yang J. Dynamic response and energy absorption of functionally graded porous structures. Materials and Design, 2018, 140:473-487.
[44] Cheng X, Zhang Y, Ren X, et al. Design and mechanical characteristics of auxetic metamaterial with tunable stiffness. International Journal of Mechanical Sciences, 2022, 223:107286.
[45] Wang SL, Wang HQ, Ding YY, et al. Crushing behavior and deformation mechanism of randomly honeycomb cylindrical shell structure. Thin-Walled Structures, 2020, 151:106739.
[46] Han CJ, Li Y, Wang Q, et al. Continuous functionally graded porous titanium scaffolds manufactured by selective laser melting for bone implants. Journal of the Mechanical Behavior of Biomedical Materials, 2018, 80:119-127.
[47] Zhang XY, Fang G, Leeflang S, et al. Topological design, permeability and mechanical behavior of additively manufactured functionally graded porous metallic biomaterials. Acta Biomaterialia, 2019, 84:437-452.
[48] Tan CL, Zou J, Li S, et al. Additive manufacturing of bio-inspired multi-scale hierarchically strengthened lattice structures. International Journal of Machine Tools and Manufacture, 2021, 167:103764.
[49] Kanwar S, Vijayavenkataraman S. 3D printable bone-mimicking functionally gradient stochastic scaffolds for tissue engineering and bone implant applications. Materials and Design, 2022, 223:111199.
[50] Sharma D, Hiremath SS. Compressive and flexural properties of the novel lightweight tailored bio-inspired structures. Thin-Walled Structures, 2022, 174:109169.
[51] Li C, Yang J, Shen HS. Postbuckling of pressure-loaded auxetic sandwich cylindrical shells with FG-GRC facesheets and 3D double-V meta-lattice core. Thin-Walled Structures, 2022, 177:109440.
[52] Darabi A, Leamy MJ. Analysis and experimental validation of an optimized gradient-index phononic-crystal lens. Physical Review Applied, 2018, 10(2):024045.
[53] Hyun J, Choi W, Kim M. Gradient-index phononic crystals for highly dense flexural energy harvesting. Applied Physics Letters, 2019, 115(17):173901.
[54] Wang S, Gao F, Hu YX, et al. Skin-inspired tactile sensor based on gradient pore structure enable broad range response and ultrahigh pressure resolution. Chemical Engineering Journal, 2022, 443:136446.
[55] Pan DK, Xu YL, Li WB, et al. Novel rotational motion actuated beam-type multistable metastructures. Materials and Design, 2022, 224:111309.
[56] Ninh DG, Ha NH, Long NT, et al. Thermal vibrations of complex-generatrix shells made of sandwich CNTRC sheets on both sides and open/closed cellular functionally graded porous core. Thin-Walled Structures, 2023, 182:110161.
[57] Alomarah A, Masood SH, Ruan D. Metamaterials with enhanced mechanical properties and tuneable Poisson's ratio. Smart Materials and Structures, 2022, 31(2):025026.